

# Experimental Demonstration of Topological Catalysis for CO<sub>2</sub> Electroreduction

Xiangdong Kong,<sup>||</sup> Zhao Liu,<sup>||</sup> Zhigang Geng,<sup>||</sup> An Zhang, Ziyang Guo, Shengtao Cui, Chuan Xia, Shijing Tan, Shiming Zhou, Zhengfei Wang,\* and Jie Zeng\*



Cite This: *J. Am. Chem. Soc.* 2024, 146, 6536–6543



Read Online

ACCESS |



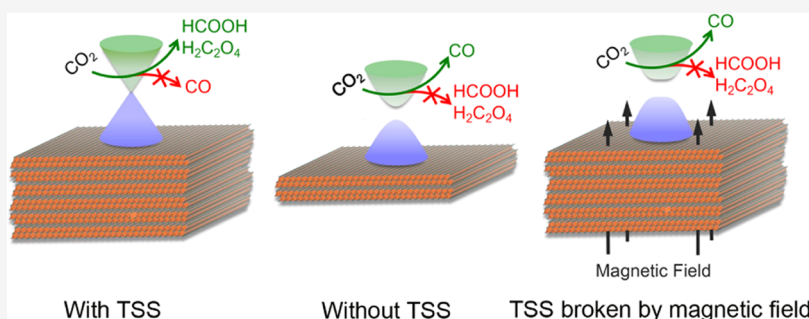
Metrics & More



Article Recommendations



Supporting Information



**ABSTRACT:** The past decade has witnessed substantial progress in understanding nontrivial band topology and discovering exotic topological materials in condensed-matter physics. Recently, topological physics has been further extended to the chemistry discipline, leading to the emergence of topological catalysis. In principle, the topological effect is detectable in catalytic reactions, but no conclusive evidence has been reported yet. Herein, by precisely manipulating the topological surface state (TSS) of Bi<sub>2</sub>Se<sub>3</sub> nanosheets through thickness control and the application of a magnetic field, we provide direct experimental evidence to illustrate topological catalysis for CO<sub>2</sub> electroreduction. With and without the cooperation of TSS, CO<sub>2</sub> is mainly reduced into liquid fuels (HCOOH and H<sub>2</sub>C<sub>2</sub>O<sub>4</sub>) and CO, exhibiting high (up to 90% at −1.1 V versus reversible hydrogen electrode) and low Faradaic efficiency (FE), respectively. Theoretically, the product and FE difference can be attributed to the TSS-regulated adsorption of key intermediates and the reduced barrier of the potential-determining step. Our work demonstrates the inherent correlation between band topology and electrocatalysis, paving a new avenue for designing high-performance catalysts.

## INTRODUCTION

Topology, a mathematical concept for continuous transformation, presents a new way to classify the electronic states in solid-state materials. Based on the topological band theory, topological materials are characterized by symmetry-protected topological surface states (TSSs), which are immune to local perturbations without breaking the bulk topology.<sup>1–3</sup> TSS-relevant quantum phenomena have been intensively studied by the physics community.<sup>4–7</sup> Recently, with the application of topological materials in the field of chemistry, a new interdisciplinary called topological catalysis has appeared.<sup>8–12</sup> In heterogeneous catalysis, the reactant adsorption, electron transfer, and product desorption are highly sensitive to the surface environment, so a robust TSS offers an exciting opportunity to design high-performance catalysts. Currently, although a variety of topological semimetal enhanced catalytic reactions<sup>13–17</sup> are reported in oxygen and hydrogen evolution reactions (OER and HER), direct experimental evidence to identify the intrinsic TSS effect in topological catalysis is still lacking.

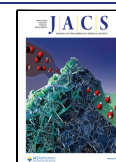
In principle, in a comparative measurement for the same catalyst with and without TSS, the product and efficiency will provide a smoking-gun signature to distinguish the intrinsic TSS effect in topological catalysis. Theoretically, the TSS can be simply eliminated by turning off the spin–orbit coupling (SOC).<sup>1–3</sup> However, the relativistic SOC effect cannot be artificially turned off in real experiments, making this comparison impossible. It is well-known that the SOC-eliminated TSS is induced by a band-inversion mechanism, which controls the topological phase transition between trivial and nontrivial states.<sup>18–20</sup> This indicates that if we can precisely suppress the TSS while keeping the local surface environment unchanged in a catalytic reaction, it is also possible to detect the intrinsic TSS effect. As one of the three-

**Received:** October 8, 2023

**Revised:** February 6, 2024

**Accepted:** February 7, 2024

**Published:** February 27, 2024



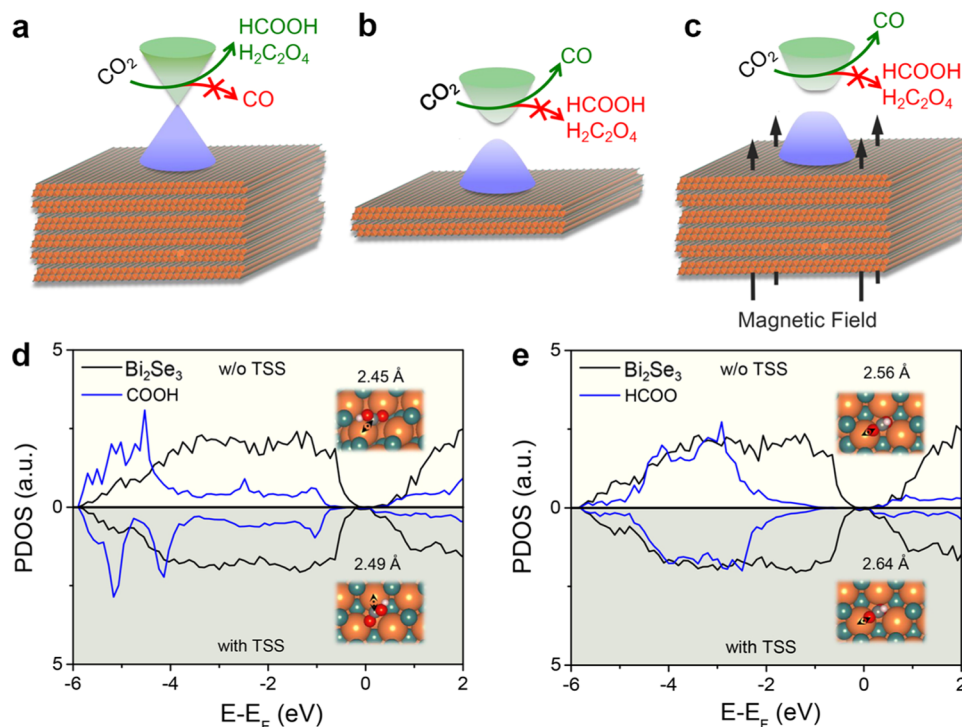


**Figure 1.** Design strategy for identifying the intrinsic TSS effect in topological catalysis. Schematic CO<sub>2</sub> electroreduction over thick Bi<sub>2</sub>Se<sub>3</sub> with (a) TSS, (b) thin Bi<sub>2</sub>Se<sub>3</sub> without TSS, and (c) thick Bi<sub>2</sub>Se<sub>3</sub> in a magnetic field without TSS. The target products and byproducts are labeled with green and red colors, respectively. The magnetic field is denoted by vertical arrows. (d) PDOS of \*COOH adsorbed on 4-QL Bi<sub>2</sub>Se<sub>3</sub> with and without TSS. The insets display the top view of the adsorption configuration and Bi–C bond length. (e) PDOS of HCOO\* adsorbed on 4-QL Bi<sub>2</sub>Se<sub>3</sub> with and without TSS. The insets display the top view of the adsorption configuration and Bi–O bond length. To guide the view, the PDOS of Bi<sub>2</sub>Se<sub>3</sub> is rescaled to the adsorbate in (d, e).

dimensional topological insulators, bismuth selenide (Bi<sub>2</sub>Se<sub>3</sub>) contains active Bi species for CO<sub>2</sub> electroreduction, where the TSS of Bi<sub>2</sub>Se<sub>3</sub> could be experimentally regulated via extrinsic methods.<sup>21,22</sup> Following this guideline, three complementary experimental schemes are designed to reveal the mysterious topological catalysis toward CO<sub>2</sub> electroreduction. In the first experiment (Figure 1a), we choose a thick Bi<sub>2</sub>Se<sub>3</sub> with a TSS. In the second experiment (Figure 1b), we choose a thin Bi<sub>2</sub>Se<sub>3</sub> without a TSS, where the TSS is eliminated by quantum confinement.<sup>21</sup> In the third experiment (Figure 1c), we choose a thick Bi<sub>2</sub>Se<sub>3</sub> but perform the catalytic reaction under a magnetic field, where the time-reversal symmetry-protected TSS is broken by a magnetic field.<sup>22</sup> Obviously, if the catalytic activity and/or dominant product in the second and third experiments are similar but different in the first experiment, it is straightforward to confirm that the intrinsic TSS effect is to tune the catalytic activity and/or selectivity.

In this work, we focus on three-dimensional (3D) TI Bi<sub>2</sub>Se<sub>3</sub><sup>23–28</sup> for CO<sub>2</sub> electroreduction to illustrate the topological effect in topological catalysis. Theoretically, we found that TSS is capable of regulating the adsorption of key intermediates in CO<sub>2</sub> electroreduction. Experimentally, we found that thick Bi<sub>2</sub>Se<sub>3</sub> (6 nm) nanosheets with TSS mainly boost CO<sub>2</sub> reduction into liquid fuels, characterized by a high geometrical current density (*j*) of 46.9 mA·cm<sup>−2</sup> at −1.1 V versus reversible hydrogen electrode (vs RHE) with a Faradaic efficiency (FE) of 60% for HCOOH and 30% for H<sub>2</sub>C<sub>2</sub>O<sub>4</sub>. However, thin Bi<sub>2</sub>Se<sub>3</sub> (2 nm) and thick Bi<sub>2</sub>Se<sub>3</sub> (6 nm) nanosheets under a magnetic field, both without TSS, mainly facilitate CO<sub>2</sub> reduction into CO, characterized by a decreased geometrical *j* and FE. This conclusive experimental evidence

directly identifies the intrinsic TSS effect in topological catalysis. Moreover, the mechanism behind the tunable catalytic activity and selectivity are also revealed by first-principles calculations, which originated from the TSS-reduced barrier of the potential-determining step (PDS). Our results establish an internal correspondence between TSS and electrocatalysis and introduce a universal extrinsic method to explore the topological effect in topological catalysis.

## RESULTS AND DISCUSSION

**Investigation of the TSS Effect on the Adsorption of Intermediates.** Before performing the electrochemical measurement, we carried out first-principles calculations for \*COOH and HCOO\* on four quintuple-layer (4-QL) Bi<sub>2</sub>Se<sub>3</sub> with and without TSS to determine whether or not the TSS has a notable effect on the adsorption of intermediates for CO<sub>2</sub> electroreduction (Figure S1). The projected density of state (PDOS) for \*COOH and HCOO\* is shown in Figure 1d,e, respectively. Comparing the PDOS with and without TSS, one can see that the TSS upshifts the occupied states of \*COOH and HCOO\* toward the Fermi level, indicating a weakened adsorption behavior. This conclusion is also supported by the calculated bond length and adsorption energy (*E*<sub>ad</sub>). For \*COOH adsorption, the TSS increases the Bi–C bond by 0.04 Å and decreases the *E*<sub>ad</sub> by 0.07 eV (inset of Figure 1d and Table S1). For HCOO\* adsorption, the TSS increases the Bi–O bond by 0.08 Å and decreases the *E*<sub>ad</sub> by 0.03 eV (inset of Figure 1e and Table S1). Therefore, the TSS of Bi<sub>2</sub>Se<sub>3</sub> has a considerable effect on the adsorption of intermediates, making it feasible to detect the TSS-regulated catalytic activity and selectivity experimentally.

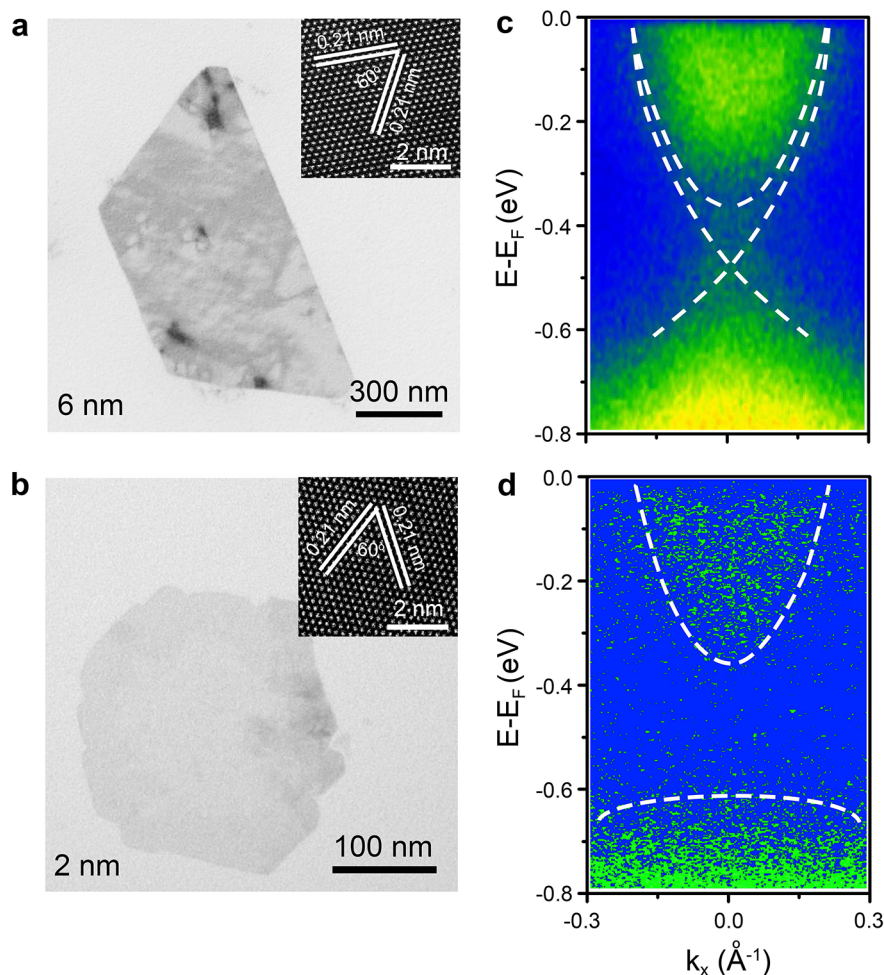


**Figure 2.** Characterizations of 6 and 2 nm  $\text{Bi}_2\text{Se}_3$  nanosheets. TEM images of (a) 6 nm and (b) 2 nm  $\text{Bi}_2\text{Se}_3$  nanosheets. Insets of (a) and (b) display HAADF-STEM images. ARPES spectra of (c) 6 nm and (d) 2 nm  $\text{Bi}_2\text{Se}_3$  nanosheets. The white dashed lines in (c) and (d) are used to guide the TSS and bulk state.

**Construction of Model Catalysts.** In order to experimentally identify the intrinsic TSS effect in topological catalysis, the high-quality single-crystal  $\text{Bi}_2\text{Se}_3$  nanosheets are synthesized by a solvothermal method.<sup>29</sup> The sample quality is determined by X-ray diffraction (XRD) (Figure S2), Raman spectroscopy (Figure S3), X-ray photoelectron spectroscopy (XPS) (Figure S4), and inductively coupled plasma-atomic emission spectroscopy (ICP-AES) (Table S2), where the characterized modes are consistent with previous work.<sup>30</sup> The gapless TSS only exists in  $\text{Bi}_2\text{Se}_3$  with enough thickness;<sup>21,31,32</sup> otherwise, it will be gapped by surface coupling. As such, we prepare two different kinds of  $\text{Bi}_2\text{Se}_3$  nanosheets (6 nm with TSS  $\sim 6$ -QL and 2 nm without TSS  $\sim 2$ -QL) to perform the comparative electrochemical experiments, where the thickness is determined by atomic force microscopy (AFM) measurement (Figure S5). The 6 and 2 nm  $\text{Bi}_2\text{Se}_3$  nanosheets are characterized by transmission electron microscopy (TEM) (Figures S6 and 2a,b), selected area electron diffraction (SAED) (Figure S7), and high-angle annular dark-field scanning transmission electron microscopy (HAADF-STEM) (insert Figure 2a,b) measurements, showing the high quality of single crystals with hexagonal structure stacking along the  $\langle 001 \rangle$  direction. To directly identify the TSS in the as-prepared samples, angle-resolved photoelectron spectroscopy (ARPES) measurements are performed.<sup>33,34</sup> In the ARPES spectra, the 6

nm  $\text{Bi}_2\text{Se}_3$  nanosheets exhibit a TSS with a Dirac cone of around  $-0.5$  eV below the Fermi level (Figure 2c), which is characterized by the spectral peak in its energy distribution curve (EDC) at the  $\Gamma$  point (Figure S8), whereas the 2 nm  $\text{Bi}_2\text{Se}_3$  nanosheets exhibit a gapped state below the Fermi level (Figure 2d). The ARPES spectral feature of 6 nm  $\text{Bi}_2\text{Se}_3$  nanosheets is in accordance with that of bulk single-crystalline  $\text{Bi}_2\text{Se}_3$  (Figure S9). These features are also consistent with ultraviolet photoelectron spectroscopy (UPS) measurements (Figure S10), where the 6 nm  $\text{Bi}_2\text{Se}_3$  nanosheets with TSS exhibit a larger signal than the 2 nm  $\text{Bi}_2\text{Se}_3$  nanosheets without TSS near the Fermi level. Accordingly, the TSS of  $\text{Bi}_2\text{Se}_3$  nanosheets is successfully switched by regulating the thickness.

**Catalytic Performance of Model Catalysts.** Based on high-quality  $\text{Bi}_2\text{Se}_3$  nanosheets with and without TSS, we further evaluate the catalytic performance. In  $\text{CO}_2$  electroreduction, the gaseous products of  $\text{H}_2$  and  $\text{CO}$  are determined by online gas chromatography measurement (Figure S11), while the liquid products of  $\text{HCOOH}$  and  $\text{H}_2\text{C}_2\text{O}_4$  are determined by nuclear magnetic resonance (Figure S12) and ion chromatography (Figure S13) analyses, respectively. Figure 3a shows the geometrical current density ( $j$ ) for  $\text{CO}_2$  electroreduction over 6 and 2 nm  $\text{Bi}_2\text{Se}_3$  nanosheets. The geometrical  $j$  monotonically increases with increasing potential, where the 6 nm  $\text{Bi}_2\text{Se}_3$  nanosheets show larger values at all



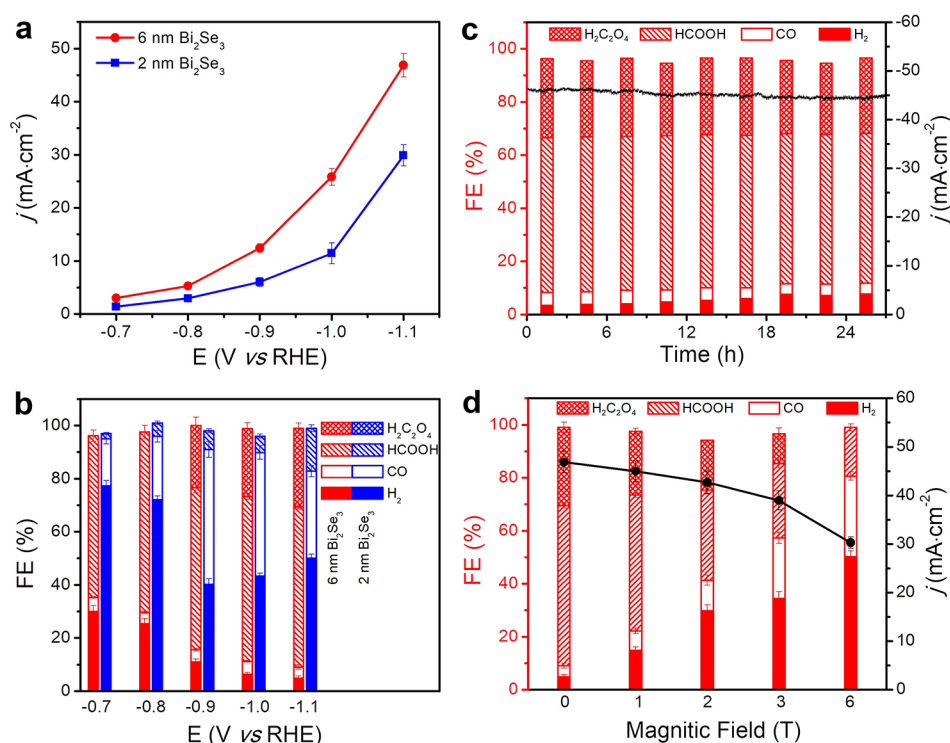


**Figure 3.** Catalytic performance of 6 and 2 nm  $\text{Bi}_2\text{Se}_3$  nanosheets toward  $\text{CO}_2$  electroreduction. (a) Geometrical  $j$  and (b) FE over 6 and 2 nm  $\text{Bi}_2\text{Se}_3$  nanosheets. (c) 27 h durability test of 6 nm  $\text{Bi}_2\text{Se}_3$  nanosheets at the potential of  $-1.1$  V vs RHE. (d) Geometrical  $j$  and FE of 6 nm  $\text{Bi}_2\text{Se}_3$  nanosheets under different magnetic fields at  $-1.1$  V vs RHE. The scale bar represents the standard deviations for three separate tests.

potentials. At  $-1.1$  V vs RHE, the geometrical  $j$  for 6 nm  $\text{Bi}_2\text{Se}_3$  nanosheets even increases up to  $46.9\text{ mA}\cdot\text{cm}^{-2}$ , which is 1.6 times as high as that ( $29.9\text{ mA}\cdot\text{cm}^{-2}$ ) for 2 nm  $\text{Bi}_2\text{Se}_3$  nanosheets. The intrinsic activity for the 6 and 2 nm  $\text{Bi}_2\text{Se}_3$  nanosheets is also investigated. Derived by the cyclic voltammogram (CV) technique under different scan rates, the electrochemical active surface area (ECSA) of the 2 and 6 nm  $\text{Bi}_2\text{Se}_3$  nanosheets is determined by measuring the double-layer capacitance ( $C_{dl}$ ) (Figure S14). The geometrical  $j$  is normalized by  $C_{dl}$  for 2 and 6 nm  $\text{Bi}_2\text{Se}_3$  nanosheets toward  $\text{CO}_2$  electroreduction, where the normalized geometrical  $j$  for 6 nm  $\text{Bi}_2\text{Se}_3$  nanosheets is still higher than that of 2 nm  $\text{Bi}_2\text{Se}_3$  nanosheets at all potentials (Figure S15). This is also consistent with the electrochemical impedance spectroscopy measurement, where 6 nm  $\text{Bi}_2\text{Se}_3$  nanosheets exhibit a smaller charge-transfer resistance ( $R_{CT}$ ) than 2 nm  $\text{Bi}_2\text{Se}_3$  nanosheets (Figure S16). As shown in Figure S17, carbon black nanoparticles exhibited an FE for  $\text{H}_2$  higher than 95.3% at all applied potentials, suggesting that carbon black nanoparticles do not contribute to the regulation of the catalytic performance of  $\text{Bi}_2\text{Se}_3$  nanosheets. Generally, the size effect can regulate the catalytic performance of nanocatalysts.<sup>35–37</sup> To rule out this effect from our experiment, we further adopt 10 and 14 nm  $\text{Bi}_2\text{Se}_3$  nanosheets (Figures S18 and S19) as catalysts toward  $\text{CO}_2$  electroreduction. It is believed that thin nanosheets with a large specific surface area will have a high catalytic activity.<sup>38</sup> However, our results demonstrate that the catalytic activities for 6, 10, and 14 nm  $\text{Bi}_2\text{Se}_3$  nanosheets follow the universal trend of size effect (Figures S20–S22), whereas 2 nm  $\text{Bi}_2\text{Se}_3$  nanosheets do not follow this trend. Therefore, the drastic activity difference between 6 and 2 nm  $\text{Bi}_2\text{Se}_3$  nanosheets should be attributed to the presence and absence of the TSS rather than the size effect.

Besides the geometrical  $j$ , the product distributions of  $\text{CO}_2$  electroreduction are also sensitive to the thickness of the  $\text{Bi}_2\text{Se}_3$  nanosheets. Three significant characteristics can be observed in our measurement, as shown in Figure 3b. (1) For 6 nm  $\text{Bi}_2\text{Se}_3$  nanosheets, the dominant product is liquid fuels ( $\text{HCOOH}$  and  $\text{H}_2\text{C}_2\text{O}_4$ ) with high FE at all potentials, whereas for 2 nm  $\text{Bi}_2\text{Se}_3$  nanosheets, the dominant product is  $\text{CO}$  with low FE at all potentials. (2) For 6 nm  $\text{Bi}_2\text{Se}_3$  nanosheets,  $\text{HCOOH}$  exists at all potentials, but  $\text{H}_2\text{C}_2\text{O}_4$  exists only at high potentials ( $-0.9$ ,  $-1.0$ , and  $-1.1$  V vs RHE). (3) For 2 nm  $\text{Bi}_2\text{Se}_3$  nanosheets,  $\text{HCOOH}$  exists at all potentials, but  $\text{H}_2\text{C}_2\text{O}_4$  does not exist. At  $-1.1$  V vs RHE, the FE for carbonaceous products over 6 nm  $\text{Bi}_2\text{Se}_3$  nanosheets increases up to 94% (60%  $\text{HCOOH}$ , 30%  $\text{H}_2\text{C}_2\text{O}_4$ , and 4%  $\text{CO}$ ), which is 1.9 times as high as that (49%) for 2 nm  $\text{Bi}_2\text{Se}_3$  nanosheets, representing one of the best catalysts for  $\text{CO}_2$  electroreduction (Table S3). Control electrolysis under an Ar atmosphere revealed that the carbonaceous products originated solely from gaseous  $\text{CO}_2$  (Figure S23). Moreover, bulk  $\text{Bi}_2\text{Se}_3$  exhibited a distribution of products similar to 6 nm  $\text{Bi}_2\text{Se}_3$  nanosheets, further suggesting the regulation of TSS on  $\text{CO}_2$  electroreduction (Figure S24). To test the stability of 6 nm  $\text{Bi}_2\text{Se}_3$  nanosheets, a static measurement is performed at  $-1.1$  V vs RHE. During 27 h continuous reactions, the decay of geometrical  $j$  is less than 6%, and the FE values of  $\text{HCOOH}$  and  $\text{H}_2\text{C}_2\text{O}_4$  remain higher than 56% and 27%, respectively (Figure 3c). Based on both post-reaction and in situ characterizations, the phase and morphology for both 6 and 2 nm  $\text{Bi}_2\text{Se}_3$  nanosheets remain intact during  $\text{CO}_2$  electroreduction (Figures S25–S28). Furthermore, the  $\text{CO}_2$  electroreduction over 6 nm  $\text{Bi}_2\text{Se}_3$  nanosheets is in situ conducted under a magnetic field (Figure S29). As the intensity of the magnetic field increases from 0 to 6 T at  $-1.1$  V vs RHE (Figure 3d), the geometrical  $j$  decreases

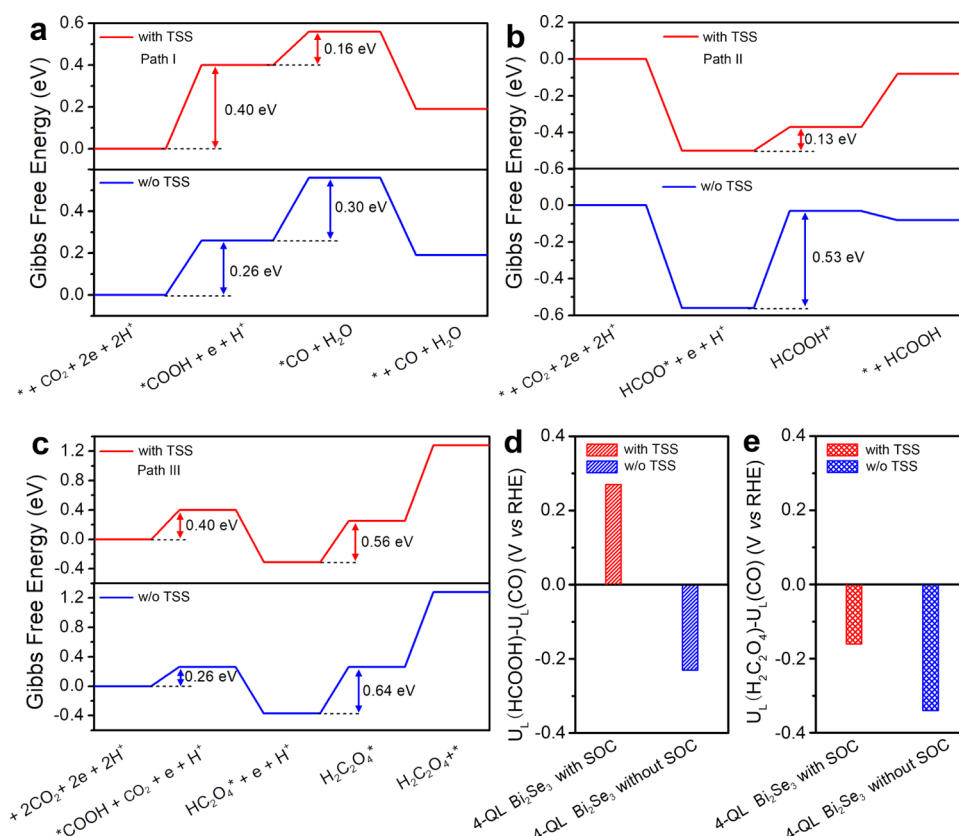


**Figure 4.** Tunable catalytic activity and selectivity by TSS. Gibbs free energy diagrams for (a) CO<sub>2</sub> reduction into CO, (b) HCOOH, and (c) H<sub>2</sub>C<sub>2</sub>O<sub>4</sub> with and without TSS. Thermodynamic limiting potential difference between (d) HCOOH and CO and (e) H<sub>2</sub>C<sub>2</sub>O<sub>4</sub> and CO with and without TSS.

from 46.9 to 30.3 mA·cm<sup>-2</sup>. Meanwhile, the FE for liquid fuels reduces from 90% (HCOOH and H<sub>2</sub>C<sub>2</sub>O<sub>4</sub>) to 18% (HCOOH). Clearly, by applying the magnetic field, the reduced activity and changed dominant product (from liquid fuels to CO) makes 6 nm Bi<sub>2</sub>Se<sub>3</sub> nanosheets more similar to 2 nm Bi<sub>2</sub>Se<sub>3</sub> nanosheets (Figures S30 and S31). Nevertheless, the catalytic activity and product distribution for 2 nm Bi<sub>2</sub>Se<sub>3</sub> nanosheets remain almost steady in all applied magnetic fields (Figure S32), revealing that the magnetic field itself cannot change the catalytic performance. The comparison of total *j* for both 6 and 2 nm Bi<sub>2</sub>Se<sub>3</sub> nanosheets with/without a magnetic field revealed that the elimination of TSS significantly altered the catalytic activity (Figure S33). Based on the analysis of in situ attenuated total reflectance surface-enhanced infrared absorption spectroscopy (ATR-SEIRAS) spectra, the variation of product distribution is also related to different adsorbed configurations of reaction intermediates on 6 and 2 nm Bi<sub>2</sub>Se<sub>3</sub> nanosheets (Figures S34 and S35). This complementary experimental evidence demonstrates that both the activity and the selectivity of CO<sub>2</sub> electroreduction are tunable by the TSS of Bi<sub>2</sub>Se<sub>3</sub> nanosheets, directly identifying the intrinsic TSS effect in topological catalysis.

**Theoretical Investigation of the Reaction Mechanism.** To gain theoretical insights into the TSS effect on CO<sub>2</sub> electroreduction, we systematically calculate the variation of Gibbs free energy ( $\Delta G$ ) in the conversion of CO<sub>2</sub> into CO, HCOOH, and H<sub>2</sub>C<sub>2</sub>O<sub>4</sub>. The 4-QL Bi<sub>2</sub>Se<sub>3</sub> slabs with and without the application of SOC are adopted to represent the Bi<sub>2</sub>Se<sub>3</sub> with and without TSS, respectively. In our calculations, the TSS is robust to all adsorbates<sup>39</sup> (Figure S36). The

optimized structures and calculation parameters for the adsorbed intermediates are presented in Figure S37 and Tables S4–S6. Figure 4a–c shows Gibbs free energy diagrams for the formation of CO, HCOOH, and H<sub>2</sub>C<sub>2</sub>O<sub>4</sub> on 4-QL Bi<sub>2</sub>Se<sub>3</sub> slab with and without TSS, respectively. The  $\Delta G$  for the formation of \*COOH is 0.40 eV on Bi<sub>2</sub>Se<sub>3</sub> with TSS, which is 0.14 eV higher than that of Bi<sub>2</sub>Se<sub>3</sub> without TSS (0.26 eV). In contrast, the  $\Delta G$  for the formation of HCOO\* with TSS (0.13 eV) is 0.40 eV lower than that without TSS (0.53 eV). For the formation of H<sub>2</sub>C<sub>2</sub>O<sub>4</sub>, two reaction paths, including CO<sub>2</sub> coupling with \*COOH (path-III) and coupling between coadsorbed \*COOH, are considered (Figure S38). As shown in Figure 4c, the  $\Delta G$  for the formation of H<sub>2</sub>C<sub>2</sub>O<sub>4</sub>\* is calculated to be 0.56 eV on Bi<sub>2</sub>Se<sub>3</sub> with TSS, which is 0.08 eV lower than that of Bi<sub>2</sub>Se<sub>3</sub> without TSS (0.64 eV). Therefore, liquid products, including HCOOH and H<sub>2</sub>C<sub>2</sub>O<sub>4</sub>, are more favorable than CO during CO<sub>2</sub> electroreduction on Bi<sub>2</sub>Se<sub>3</sub> with TSS. The highest  $\Delta G$  of PDS for the formation of H<sub>2</sub>C<sub>2</sub>O<sub>4</sub> suggested that high potential is required for the formation of H<sub>2</sub>C<sub>2</sub>O<sub>4</sub> over 6 nm Bi<sub>2</sub>Se<sub>3</sub> nanosheets.<sup>40,41</sup> The thermodynamic limiting potential difference between the target product and byproduct (defined as  $\Delta U_L = U_L(\text{target product}) - U_L(\text{byproduct})$ , where  $U_L = -\Delta G/e$  ( $\Delta G$  is the energy barrier of PDS))<sup>42</sup> was further adopted to evaluate the product selectivity. A more positive value of  $\Delta U_L$  corresponds to a higher selectivity of the target product. Figure 4d shows the  $\Delta U_L$  between HCOOH and CO, which are 0.27 and -0.23 V vs RHE for Bi<sub>2</sub>Se<sub>3</sub> with and without TSS, respectively. Figure 4e shows the  $\Delta U_L$  between H<sub>2</sub>C<sub>2</sub>O<sub>4</sub> and CO, which are -0.16 and -0.34 V vs RHE with and without TSS, respectively. In

both cases, the  $\Delta U_L$  is more positive with TSS than without TSS, further supporting the fact that TSS tunes activity and selectivity for CO<sub>2</sub> electroreduction.

## CONCLUSIONS

In conclusion, combining the electrochemical measurements and first-principles calculations, we provide conclusive experimental evidence to directly identify the topological catalysis for CO<sub>2</sub> electroreduction and confirm the tunable catalytic activity and selectivity by TSS. Our work not only opens a new door for investigating topological effects in topological catalysis but also paves a new way for searching high-performance catalysts in topological materials.

## ASSOCIATED CONTENT

### Supporting Information

The Supporting Information is available free of charge at <https://pubs.acs.org/doi/10.1021/jacs.3c11088>.

Experimental details for the DFT calculation, synthesis of catalysts, catalyst characterization (XRD, Raman spectroscopy, XPS, SAED patterns, AFM, HRTEM, and UPS), product quantification,  $C_{dl}$  measurements, Nyquist plots, characterization after stability test, control electrolysis, in situ experiments, illustration of magnetic field experiments, and DFT models (PDF)

## AUTHOR INFORMATION

### Corresponding Authors

**Zhengfei Wang** – Hefei National Research Center for Physical Sciences at the Microscale, Key Laboratory of Strongly-Coupled Quantum Matter Physics of Chinese Academy of Sciences, Key Laboratory of Surface and Interface Chemistry and Energy Catalysis of Anhui Higher Education Institutes, Department of Chemical Physics, Hefei National Laboratory, University of Science and Technology of China, Hefei, Anhui 230026, P. R. China; [orcid.org/0000-0002-0788-9725](https://orcid.org/0000-0002-0788-9725); Email: [zfwang15@ustc.edu.cn](mailto:zfwang15@ustc.edu.cn)

**Jie Zeng** – Hefei National Research Center for Physical Sciences at the Microscale, Key Laboratory of Strongly-Coupled Quantum Matter Physics of Chinese Academy of Sciences, Key Laboratory of Surface and Interface Chemistry and Energy Catalysis of Anhui Higher Education Institutes, Department of Chemical Physics, Hefei National Laboratory, University of Science and Technology of China, Hefei, Anhui 230026, P. R. China; School of Chemistry & Chemical Engineering, Anhui University of Technology, Ma'anshan, Anhui 243002, P. R. China; [orcid.org/0000-0002-8812-0298](https://orcid.org/0000-0002-8812-0298); Email: [zzengj@ustc.edu.cn](mailto:zzengj@ustc.edu.cn)

### Authors

**Xiangdong Kong** – Hefei National Research Center for Physical Sciences at the Microscale, Key Laboratory of Strongly-Coupled Quantum Matter Physics of Chinese Academy of Sciences, Key Laboratory of Surface and Interface Chemistry and Energy Catalysis of Anhui Higher Education Institutes, Department of Chemical Physics, Hefei National Laboratory, University of Science and Technology of China, Hefei, Anhui 230026, P. R. China

**Zhao Liu** – Hefei National Research Center for Physical Sciences at the Microscale, Key Laboratory of Strongly-Coupled Quantum Matter Physics of Chinese Academy of Sciences, Key Laboratory of Surface and Interface Chemistry

and Energy Catalysis of Anhui Higher Education Institutes, Department of Chemical Physics, Hefei National Laboratory, University of Science and Technology of China, Hefei, Anhui 230026, P. R. China

**Zhigang Geng** – Hefei National Research Center for Physical Sciences at the Microscale, Key Laboratory of Strongly-Coupled Quantum Matter Physics of Chinese Academy of Sciences, Key Laboratory of Surface and Interface Chemistry and Energy Catalysis of Anhui Higher Education Institutes, Department of Chemical Physics, Hefei National Laboratory, University of Science and Technology of China, Hefei, Anhui 230026, P. R. China; [orcid.org/0000-0003-3183-5900](https://orcid.org/0000-0003-3183-5900)

**An Zhang** – Hefei National Research Center for Physical Sciences at the Microscale, Key Laboratory of Strongly-Coupled Quantum Matter Physics of Chinese Academy of Sciences, Key Laboratory of Surface and Interface Chemistry and Energy Catalysis of Anhui Higher Education Institutes, Department of Chemical Physics, Hefei National Laboratory, University of Science and Technology of China, Hefei, Anhui 230026, P. R. China

**Ziyang Guo** – Hefei National Research Center for Physical Sciences at the Microscale, Key Laboratory of Strongly-Coupled Quantum Matter Physics of Chinese Academy of Sciences, Key Laboratory of Surface and Interface Chemistry and Energy Catalysis of Anhui Higher Education Institutes, Department of Chemical Physics, Hefei National Laboratory, University of Science and Technology of China, Hefei, Anhui 230026, P. R. China

**Shengtao Cui** – Hefei National Research Center for Physical Sciences at the Microscale, Key Laboratory of Strongly-Coupled Quantum Matter Physics of Chinese Academy of Sciences, Key Laboratory of Surface and Interface Chemistry and Energy Catalysis of Anhui Higher Education Institutes, Department of Chemical Physics, Hefei National Laboratory, University of Science and Technology of China, Hefei, Anhui 230026, P. R. China

**Chuan Xia** – School of Materials and Energy, University of Electronic Science and Technology of China, Chengdu, Sichuan 611731, P. R. China; [orcid.org/0000-0003-4526-159X](https://orcid.org/0000-0003-4526-159X)

**Shijing Tan** – Hefei National Research Center for Physical Sciences at the Microscale, Key Laboratory of Strongly-Coupled Quantum Matter Physics of Chinese Academy of Sciences, Key Laboratory of Surface and Interface Chemistry and Energy Catalysis of Anhui Higher Education Institutes, Department of Chemical Physics, Hefei National Laboratory, University of Science and Technology of China, Hefei, Anhui 230026, P. R. China; [orcid.org/0000-0002-8537-9528](https://orcid.org/0000-0002-8537-9528)

**Shiming Zhou** – Hefei National Research Center for Physical Sciences at the Microscale, Key Laboratory of Strongly-Coupled Quantum Matter Physics of Chinese Academy of Sciences, Key Laboratory of Surface and Interface Chemistry and Energy Catalysis of Anhui Higher Education Institutes, Department of Chemical Physics, Hefei National Laboratory, University of Science and Technology of China, Hefei, Anhui 230026, P. R. China; [orcid.org/0000-0002-1597-6060](https://orcid.org/0000-0002-1597-6060)

Complete contact information is available at: <https://pubs.acs.org/10.1021/jacs.3c11088>

### Author Contributions

<sup>||</sup>X.K., Z.L., and Z.G. contributed equally to this work.



## Notes

The authors declare no competing financial interest.

## ■ ACKNOWLEDGMENTS

This work was supported by the National Key Research and Development Program of China (2021YFA1500500), the CAS Project for Young Scientists in Basic Research (YSBR-051), the National Science Fund for Distinguished Young Scholars (21925204), the National Natural Science Foundation of China (U19A2015, 22221003, 22250007, 22322901, 12174369, 11774325, and 22209163), the Innovation Program for Quantum Science and Technology (2021ZD0302800), the Fundamental Research Funds for the Central Universities, the Collaborative Innovation Program of Hefei Science Center, CAS (2022HSC-CIP004), the International Partnership Program of Chinese Academy of Sciences (123GJHZ2022101GC), the Youth Project of Anhui Natural Science Foundation (2208085QB43), and the University of Electronic Science and Technology of China (UESTC) for Startup funding (A1098531023601264). This work was partially carried out at the USTC Center for Micro and Nanoscale Research and Fabrication. This work was partially carried out at the Instruments Center for Physical Science, University of Science and Technology of China. The authors thank the Supercomputing Center at USTC for providing the computing resources. A portion of this work was performed on the Steady High Magnetic Field Facilities (SM1 superconducting magnet), High Magnetic Field Laboratory, CAS. The authors thank the ARPES Endstation in the NSRL for providing ARPES measurements.

## ■ REFERENCES

- (1) Hasan, M. Z.; Kane, C. L. *Colloquium: Topological insulators. Rev. Mod. Phys.* **2010**, *82*, 3045–3067.
- (2) Bansil, A.; Lin, H.; Das, T. *Colloquium: Topological band theory. Rev. Mod. Phys.* **2016**, *88*, No. 021004.
- (3) Armitage, N. P.; Mele, E. J.; Vishwanath, A. Weyl and Dirac semimetals in three-dimensional solids. *Rev. Mod. Phys.* **2018**, *90*, No. 015001.
- (4) Klitzing, K. V.; Dorda, G.; Pepper, M. New method for high-accuracy determination of the fine-structure constant based on quantized hall resistance. *Phys. Rev. Lett.* **1980**, *45*, 494–497.
- (5) König, M.; Wiedmann, S.; Brüne, C.; Roth, A.; Buhmann, H.; Molenkamp, L. W.; Qi, X.-L.; Zhang, S.-C. Quantum spin hall insulator state in HgTe quantum wells. *Science* **2007**, *318*, 766–770.
- (6) Chang, C.-Z.; Zhang, J.; Feng, X.; Shen, J.; Zhang, Z.; Guo, M.; Li, K.; Ou, Y.; Wei, P.; Wang, L.-L.; Ji, Z.-Q.; Feng, Y.; Ji, S.; Chen, X.; Jia, J.; Dai, X.; Fang, Z.; Zhang, S.-C.; He, K.; Wang, Y.; Lu, L.; Ma, X.-C.; Xue, Q.-K. Experimental observation of the quantum anomalous Hall effect in a magnetic topological insulator. *Science* **2013**, *340*, 167–170.
- (7) Xu, S.-Y.; Belopolski, I.; Alidoust, N.; Neupane, M.; Bian, G.; Zhang, C.; Sankar, R.; Chang, G.; Yuan, Z.; Lee, C.-C.; Huang, S.-M.; Zheng, H.; Ma, J.; Sanchez, D. S.; Wang, B.; Bansil, A.; Chou, F.; Shibaev, P. P.; Lin, H.; Jia, S.; Hasan, M. Z. Discovery of a Weyl fermion semimetal and topological Fermi arcs. *Science* **2015**, *349*, 613–617.
- (8) Luo, H.; Yu, P.; Li, G.; Yan, K. Topological quantum materials for energy conversion and storage. *Nat. Rev. Phys.* **2022**, *4*, 611–624.
- (9) Kong, D.; Cui, Y. Opportunities in chemistry and materials science for topological insulators and their nanostructures. *Nat. Chem.* **2011**, *3*, 845–849.
- (10) Xiao, J.; Kou, L.; Yam, C.-Y.; Frauenheim, T.; Yan, B. Towards rational design of catalysts supported on a topological insulator substrate. *ACS Catal.* **2015**, *5*, 7063–7067.
- (11) Wang, Z.; Lin, Z.; Wang, Y.; Shen, S.; Zhang, Q.; Wang, J.; Zhong, W. Nontrivial topological surface states in Ru<sub>3</sub>Sn<sub>7</sub> toward wide pH-range hydrogen evolution reaction. *Adv. Mater.* **2023**, *35*, No. 2302007.
- (12) Wang, S.; Ly, G. T. H.; Wahiduzzaman, M.; Simms, C.; Dovgaliuk, I.; Tissot, A.; Maurin, G.; Parac-Vogt, T. N.; Serre, C. A zirconium metal-organic framework with SOC topological net for catalytic peptide bond hydrolysis. *Nat. Commun.* **2022**, *13*, No. 1284.
- (13) Rajamathi, C. R.; Gupta, U.; Kumar, N.; Yang, H.; Sun, Y.; Süß, V.; Shekhar, C.; Schmidt, M.; Blumtritt, H.; Werner, P.; Yan, B.; Parkin, S.; Felser, C.; Rao, C. N. R. Weyl semimetals as hydrogen evolution catalysts. *Adv. Mater.* **2017**, *29*, No. 1606202.
- (14) Li, G.; Xu, Q.; Shi, W.; Fu, C.; Jiao, L.; Kamminga, M. E.; Yu, M.; Tüysüz, H.; Kumar, N.; Süß, V.; Saha, R.; Srivastava, A. K.; Wirth, S.; Auffermann, G.; Gooth, J.; Parkin, S.; Sun, Y.; Liu, E.; Felser, C. Surface states in bulk single crystal of topological semimetal Co<sub>3</sub>Sn<sub>2</sub>S<sub>2</sub> toward water oxidation. *Sci. Adv.* **2019**, *5*, No. eaaw9867, DOI: 10.1126/sciadv.aaw9867.
- (15) Li, G.; Fu, C.; Shi, W.; Jiao, L.; Wu, J.; Yang, Q.; Saha, R.; Kamminga, M. E.; Srivastava, A. K.; Liu, E.; Yazdani, A. N.; Kumar, N.; Zhang, J.; Blake, G. R.; Liu, X.; Fahlman, M.; Wirth, S.; Auffermann, G.; Gooth, J.; Parkin, S.; Madhavan, V.; Feng, X.; Sun, Y.; Felser, C. Dirac nodal arc semimetal PtSn<sub>4</sub>: an ideal platform for understanding surface properties and catalysis for hydrogen evolution. *Angew. Chem., Int. Ed.* **2019**, *58*, 13107–13112.
- (16) Jiang, M.-C.; Guo, G. Y.; Hirayama, M.; Yu, T.; Nomoto, T.; Arita, R. Efficient hydrogen evolution reaction due to topological polarization. *Phys. Rev. B* **2022**, *106*, No. 165120.
- (17) Samanta, M.; Tan, H.; Laha, S.; Vignolo-González, H. A.; Grunenberg, L.; Bette, S.; Duppl, V.; Schützendübe, P.; Goudar, A.; Yan, B.; Lotsch, B. V. The weyl semimetals M<sub>2</sub>IrTe<sub>4</sub> (M = Nb, Ta) as efficient catalysts for dye-sensitized hydrogen evolution. *Adv. Energy Mater.* **2023**, *13*, No. 2300503.
- (18) Bernevig, B. A.; Huges, T. L.; Zhang, S.-C. Quantum spin Hall effect and topological phase transition in HgTe quantum wells. *Science* **2006**, *314*, 1757–1761.
- (19) Young, S. M.; Chowdhury, S.; Walter, E. J.; Mele, E. J.; Kane, C. L.; Rappe, A. M. Theoretical investigation of the evolution of the topological phase of Bi<sub>2</sub>Se<sub>3</sub> under mechanical strain. *Phys. Rev. B* **2011**, *84*, No. 085106.
- (20) Weng, H.; Yu, R.; Hu, X.; Dai, X.; Fang, Z. Quantum anomalous Hall effect and related topological electronic states. *Adv. Phys.* **2015**, *64*, 227–282.
- (21) Zhang, Y.; He, K.; Chang, C.-Z.; Song, C.-L.; Wang, L.-L.; Chen, X.; Jia, J.-F.; Fang, Z.; Dai, X.; Shan, W.-Y.; Shen, S.-Q.; Niu, Q.; Qi, X.-L.; Zhang, S.-C.; Ma, X.-C.; Xue, Q.-K. Crossover of the three-dimensional topological insulator Bi<sub>2</sub>Se<sub>3</sub> to the two-dimensional limit. *Nat. Phys.* **2010**, *6*, 584–588, DOI: 10.1038/nphys1689.
- (22) Fu, Y. S.; Hanaguri, T.; Igarashi, K.; Kawamura, M.; Bahramy, M. S.; Sasagawa, T. Observation of Zeeman effect in topological surface state with distinct material dependence. *Nat. Commun.* **2016**, *7*, No. 10829.
- (23) Chen, Y. L.; Analytis, J. G.; Chu, J.-H.; Liu, Z. K.; Mo, S.-K.; Qi, L. X.; Zhang, H. J.; Lu, D. H.; Dai, X.; Fang, Z.; Zhang, S. C.; Fisher, I. R.; Hussain, Z.; Shen, Z.-X. Experimental realization of a three-dimensional topological insulator, Bi<sub>2</sub>Te<sub>3</sub>. *Science* **2009**, *325*, 178–181.
- (24) Xia, Y.; Qian, D.; Hsieh, D.; Wray, L.; Pal, A.; Lin, H.; Bansil, A.; Grauer, D.; Hor, Y. S.; Cava, R. J.; Hasan, M. Z. Observation of a large-gap topological-insulator class with a single Dirac cone on the surface. *Nat. Phys.* **2009**, *5*, 398–402.
- (25) Zhang, H.; Liu, C. X.; Qi, X. L.; Dai, X.; Fang, Z.; Zhang, S. C. Topological insulators in Bi<sub>2</sub>Se<sub>3</sub>, Bi<sub>2</sub>Te<sub>3</sub> and Sb<sub>2</sub>Te<sub>3</sub> with a single Dirac cone on the surface. *Nat. Phys.* **2009**, *5*, 438–442.
- (26) Yashina, L. V.; Sánchez-Barriga, J.; Scholz, M. R.; Volykhov, A. A.; Sirotna, A. P.; Neudachina, V. S.; Tamm, M. E.; Varykhalov, A.; Marchenko, D.; Springholz, G.; Bauer, G.; Knop-Gericke, A.; Rader, O. Negligible surface reactivity of topological insulators Bi<sub>2</sub>Se<sub>3</sub> and

Bi<sub>2</sub>Te<sub>3</sub> towards oxygen and water. *ACS Nano* **2013**, *7*, 5181–5191, DOI: 10.1021/nn400908b.

(27) Koleini, M.; Frauenheim, T.; Yan, B. Gas doping on the topological insulator Bi<sub>2</sub>Se<sub>3</sub> surface. *Phys. Rev. Lett.* **2013**, *110*, No. 016403.

(28) Rajamathi, C. R.; Gupta, U.; Pal, K.; Kumar, N.; Yang, H.; Sun, Y.; Shekhar, C.; Yan, B.; Parkin, S.; Waghmare, U. V.; Felser, C.; Rao, C. N. R. Photochemical water splitting by bismuth chalcogenide topological insulators. *ChemPhysChem* **2017**, *18*, 2322–2327.

(29) Zhuang, A.; Li, J. J.; Wang, Y. C.; Wen, X.; Lin, Y.; Xiang, B.; Wang, X.; Zeng, J. Screw-dislocation-driven bidirectional spiral growth of Bi<sub>2</sub>Se<sub>3</sub> nanoplates. *Angew. Chem., Int. Ed.* **2014**, *53*, 6425–6429.

(30) Zhao, Y.; Luo, X.; Zhang, J.; Wu, J.; Bai, X.; Wang, M.; Jia, J.; Peng, H.; Liu, Z.; Quek, S. Y.; Xiong, Q. Interlayer vibrational modes in few-quintuple-layer Bi<sub>2</sub>Te<sub>3</sub> and Bi<sub>2</sub>Se<sub>3</sub> two-dimensional crystals: Raman spectroscopy and first-principles studies. *Phys. Rev. B* **2014**, *90*, No. 245428.

(31) He, L.; Xiu, F.; Yu, X.; Teague, M.; Jiang, W.; Fan, Y.; Kou, X.; Lang, M.; Wang, Y.; Huang, G.; Yeh, N.-C.; Wang, K. L. Surface-dominated conduction in a 6 nm thick Bi<sub>2</sub>Se<sub>3</sub> thin film. *Nano Lett.* **2012**, *12*, 1486–1490, DOI: 10.1021/nl204234j.

(32) Li, N.; Sun, Y.; Sun, R.; Yang, X.; Zhang, W.; Xie, Z.; Liu, J.; Li, Y.; Li, Y.; Gong, Z.; Zhang, X.; He, W.; Cheng, Z. Topological surface state enhanced ultrafast spin dynamics of Fe/Bi<sub>2</sub>Se<sub>3</sub> heterostructures. *Phys. Rev. B* **2022**, *105*, No. 144415.

(33) Ju, S.; Bai, W.; Wu, L.; Lin, H.; Xiao, C.; Cui, S.; Li, Z.; Kong, S.; Liu, Y.; Liu, D.; Zhang, G.; Sun, Z.; Xie, Y. Evidence for itinerant carriers in an anisotropic narrow-gap semiconductor by angle-resolved photoemission spectroscopy. *Adv. Mater.* **2018**, *30*, No. 1704733.

(34) Lin, Z.; Wang, C.; Wang, P.; Yi, S.; Li, L.; Zhang, Q.; Wang, Y.; Wang, Z.; Huang, H.; Sun, Y.; Huang, Y.; Shen, D.; Feng, D.; Sun, Z.; Cho, J.-H.; Zeng, C.; Zhang, Z. Dirac fermions in antiferromagnetic FeSn kagome lattices with combined space inversion and time-reversal symmetry. *Phys. Rev. B* **2020**, *102*, No. 155103.

(35) Rong, W.; Zou, H.; Zang, W.; Xi, S.; Wei, S.; Long, B.; Hu, J.; Ji, Y.; Duan, L. Size-dependent activity and selectivity of atomic-level copper nanoclusters during CO/CO<sub>2</sub> electroreduction. *Angew. Chem., Int. Ed.* **2021**, *60*, 466–472.

(36) Wang, Z.; Wang, C.; Mao, S.; Lu, B.; Chen, Y.; Zhang, X.; Chen, Z.; Wang, Y. Decoupling the electronic and geometric effects of Pt catalysts in selective hydrogenation reaction. *Nat. Commun.* **2022**, *13*, No. 3561.

(37) Zhang, X.; Sun, Z.; Jin, R.; Zhu, C.; Zhao, C.; Lin, Y.; Guan, Q.; Cao, L.; Wang, H.; Li, S.; Yu, H.; Liu, X.; Wang, L.; Wei, S.; Li, W.-X.; Lu, J. Conjugated dual size effect of core-shell particles synergizes bimetallic catalysis. *Nat. Commun.* **2023**, *14*, No. 530.

(38) Li, X.; Wang, S.; Li, L.; Zu, X.; Sun, Y.; Xie, Y. Opportunity of atomically thin two-dimensional catalysts for promoting CO<sub>2</sub> electronreduction. *Acc. Chem. Res.* **2020**, *53*, 2964–2974.

(39) Wang, X.; Bian, G.; Miller, T.; Chiang, T.-C. Fragility of surface states and robustness of topological order in Bi<sub>2</sub>Se<sub>3</sub> against oxidation. *Phys. Rev. Lett.* **2012**, *108*, No. 096404.

(40) Angamuthu, R.; Byers, P.; Lutz, M.; Spek, A. L.; Bouwman, E. Electrocatalytic CO<sub>2</sub> conversion to oxalate by a copper complex. *Science* **2010**, *327*, 313–315.

(41) Paris, A. R.; Bocarsly, A. B. High-efficiency conversion of CO<sub>2</sub> to oxalate in water is possible using a Cr-Ga oxide electrocatalyst. *ACS Catal.* **2019**, *9*, 2324–2333.

(42) Feng, J.; Wu, L.; Liu, S.; Xu, L.; Song, X.; Zhang, L.; Zhu, Q.; Kang, X.; Sun, X.; Han, B. Improving CO<sub>2</sub>-to-C<sub>2+</sub> product electroreduction efficiency via atomic lanthanide dopant-induced tensile-strained CuO<sub>x</sub> catalysts. *J. Am. Chem. Soc.* **2023**, *145*, 9857–9866.